ETVOS: An Enhanced Total Variation Optimization Segmentation Approach for SAR Sea-Ice Image Segmentation

Tae-Jung Kwon, Jonathan Li, *Senior Member, IEEE*, and Alexander Wong, *Member, IEEE*

***Abstract*—This paper presents a novel enhanced total variation optimization segmentation (ETVOS) approach consisting of two phases to segmentation of various sea-ice types. In the total variation optimization phase, the Rudin–Osher–Fatemi total variation model was modified and implemented iteratively to estimate the piecewise constant state from a nonpiecewise constant state (the original noisy imagery) by minimizing the total variation constraints. In the finite mixture model classification phase, based on the pixel distribution, an expectation maximization method was performed to estimate the final class likelihood using a Gaussian mixture model. Then, a maximum likelihood classification technique was utilized to estimate the final class of each pixel that appeared in the product of the total variation optimization phase. The proposed method was tested on a synthetic image and various subsets of RADARSAT-2 imagery, and the results were compared with other well-established approaches. With the advantage of a short processing time, the visual inspection and quantitative analysis of segmentation results confirm the superiority of the proposed ETVOS method over other existing methods.**

***Index Terms*—Optimization, synthetic aperture radar (SAR), sea ice, segmentation, total variation.**

I. Introduction

SEA-ICE condition monitoring in polar regions is very important for various applications, including scientific research, particularly in the context of global climate changes. Sea ice has a high albedo due to its color and the fact that most of the sunlight that interacts with the sea-ice surface is reflected back into the atmosphere resulting in cold climates in polar regions. The current trend of rising temperatures in polar regions will likely warm the Arctic because of the loss of sea ice that will reduce the amount of sun rays that are reflected causing the sea ice to melt and become weakened. This trend consequently leads to a bigger problem of global climate change that will cause severe consequences to human life and Earth's natural environment. Having acknowledged the importance of sea-ice monitoring, the amount of synthetic aperture radar (SAR) sea-ice images acquired by Canada's RADARSAT-1 and -2 that are received daily at the Canadian Ice Service (CIS) and processed by trained sea-ice analysts is overwhelming. Hence, there is a great need for an automatic sea-ice monitoring system.

One of the key advantages of using SAR for sea-ice monitoring is that it uses microwave rays in the electromagnetic spectrum, which can penetrate rain, clouds, and other atmospheric substances, resulting in good monitoring capabilities during the day and night. Moreover, SAR has proved to be the most important tool for the detection of sea ice [1]–[6]. However, the segmentation of SAR sea-ice images is a very difficult task due to the presence of a multiplicative noise known as speckle. Not only does speckle noise degrade the quality of SAR images but it also makes it a very challenging task to extract tonal and texture information from images. A good example of a SAR sea-ice image adversely affected by speckle noise is shown in Fig. 1. Although there is a clear visible distinction between the two different classes, there seems to be no difference in statistical distribution of pixel values as shown in the unimodal-shaped histogram.

If the statistical distribution of pixel values forms a unimodal shape, then accurate segmentation is not possible since a computer would recognize this image as containing only one class with similar intensity values. However, this is not true as there is an apparent difference observed from Fig. 1. This behavior is believed to occur mainly due to the presence of speckle noise, which is the most influential contributing factor. Existing approaches available for automatic segmentation of SAR sea-ice images include a global histogram thresholding [7], dynamic local thresholding [8], Gamma mixture models [9], K-means clustering [10], modified neural networks [11], Markov random field model [12], and Gaussian mixture model (GMM) [13]. These methods were developed based on the investigation of global tonal characteristics from the entire image and have drawbacks and weaknesses. Mechanisms built based on global tonal characteristics tend to ignore spatial relationships between pixels, making them very difficult to implement in a highly noise-contaminated image such as SAR sea-ice images. Other conventional yet robust denoising filters such as Lee adaptive filter [14], Kuan filter [15], Frost filter [16], and speckle-reducing anisotropic diffusion method [17]

Manuscript received February 27, 2011; revised August 20, 2011 and March 22, 2012; accepted May 21, 2012. Date of publication August 31, 2012; date of current version January 17, 2013.

T.-J. Kwon is with the Department of Civil and Environmental Engineering, University of Waterloo, Waterloo, ON N2L 3G1, Canada.

J. Li is with the Key Laboratory of Underwater Acoustic Communication and Marine Information Technology of the Ministry of Education, Xiamen University, Xiamen 361005, China, and also with the Department of Geography and Environmental Management, University of Waterloo, Waterloo, ON N2L 3G1, Canada (e-mail: junli@xmu.edu.cn; junli@uwaterloo.ca).

A. Wong is with the Vision and Image Processing Research Group, Department of Systems Design Engineering, University of Waterloo, Waterloo, ON N2L 3G1, Canada.

Digital Object Identifier 10.1109/TGRS.2012.2205259

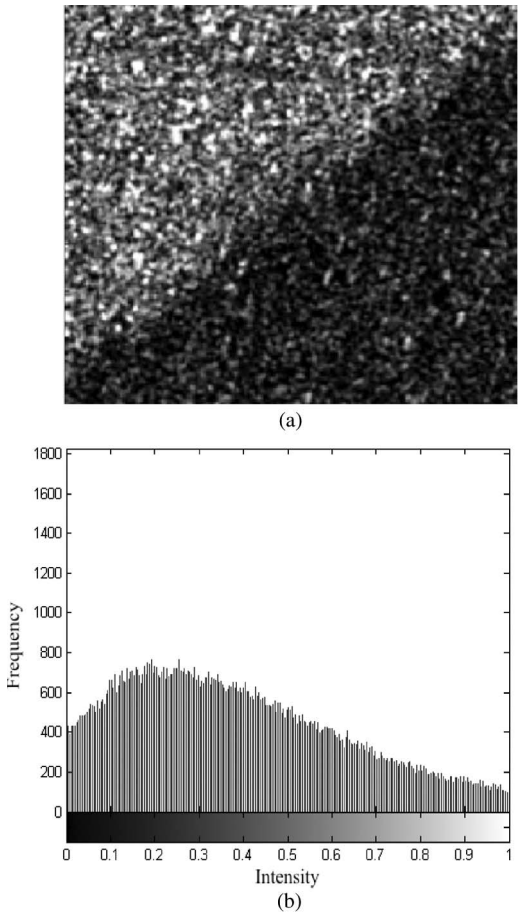

Fig. 1. (a) Subset scene from RADARSAT-2 sea-ice image. (b) Histogram generated using subset.

are widely used to denoise images prior to the application of a segmentation scheme, and many of these filters are currently available in commercial image processing software packages.

However, these methods do not perform well when particularly dealing with images that contain significant speckle noise. Apart from deriving a segmentation result by exploiting spatial and tonal relationships between pixels, other approaches to analyze texture characteristics have been studied as well [18], [19]. Moreover, some of the texture-based approaches developed so far include gray-level co-occurrence probabilities [20], [21] and Gaussian Markov random fields [22], [23]. However, these texture-based segmentation schemes have a weakness, i.e., pixels located near texture boundaries are likely to be misclassified. More importantly, some of these methods can be computationally intensive resulting in longer processing times and therefore is not well suited for operational use. Thus, the main contribution of this paper is to use a novel enhanced total variation optimization segmentation (ETVOS) approach to first reconstruct the piecewise constant state to be able to better separate the existing classes and to classify distinct features in a timely fashion.

This paper is organized as follows. The underlying methodology behind ETVOS is presented in Section II. In Section III, experimental results including data description and analysis, testing on a synthetic image, results and discussion of the proposed method, and comparison with other methods are addressed. Lastly, Section IV provides a summary of this work and recommendations for future work.

II. Methodology

The ETVOS method consists of two main phases: Phase I—extended total variation optimization—and Phase II—finite mixture model classification. In Phase I, a total variation optimization approach based on a set of constraint penalties is used to provide a rough estimate of the piecewise constant state separating the classes in the original image. In Phase II, a finite mixture model classification strategy is employed on the results from Phase I to classify distinct features including land, seawater, and various sea-ice types that appear in SAR sea-ice imagery. Thus, with the combination of the two phases together, a full and comprehensive segmentation algorithm, ETVOS, can be realized.

A. Phase I—Extended Total Variation Optimization

SAR sea-ice segmentation can be formulated as an optimization problem, where the goal is to estimate the segmented image denoted as u given the observed SAR image denoted as f by optimizing the energy function E. Let f and u be defined on discrete grids with f and u taking on nonnegative values.

One approach for solving this inverse problem is through the utilization of the Rudin–Osher–Fatemi total variation (ROFTV) model. Based on the ROFTV model, the observed SAR image f can be represented as a combination of the piecewise constant state u and noise state η as given by

$$f = u \times \eta. \tag{1}$$

In other words, by utilizing the ROFTV model, the goal is to progressively evolve a nonpiecewise constant state f, in which classes are nonseparable due to noise, artifacts, and other image details, into a piecewise constant state u where the total variation of the image is minimized and the classes are well delineated. In the process of estimating such state, the total variation minimizers in the space of function of bounded variation help preserve edges or boundaries of the objects in the image by allowing discontinuities [24]. Therefore, we are able to theoretically arrive at a clean state with sharp boundaries between different classes. Given the multiplicative relationship in (1), the problem of image segmentation can be formulated into the minimization problem based on the ROFTV model [25]. Since the original ROFTV model is expressed using a continuous formulation, it has been rewritten in a discrete form to better handle the SAR segmentation problems

$$\hat{u} = \arg\min_{u} \left[\alpha \sum_{i} |\log f(i) - \log u(i)|^2 + \beta \sum_{i} \sum_{j} \omega(i,j) \, |u(i) - u(j)| \right] \tag{2}$$

where $\log f - \log u$ represents the data fidelity term specifically designed for SAR segmentation to handle the

multiplicative nature of the underlying speckle noise, i denotes a site in the grid, ω is the weight of total variation penalty term where its value is nonnegative, $|u(i) - u(j)|$ denotes the finite intensity difference between neighboring pixels, and i and j are two interacting pixels at two different sites of the grid. The first term of (2) is to ensure that the minimized solution does not deviate from the allowed range, while the second term is the initial total variation term that penalizes pixel intensity differences within regions to enforce piecewise constant in u.

It is well understood that, by penalizing pixel intensity differences with its immediate neighbors, the edges or boundaries of the objects are better preserved but is limited in handling high noise levels. To remedy this limitation, one can take spatial closeness of pixel values into account via extending the spatial neighborhood being considered to improve statistical resilience to noise, as well as incorporating a spatial penalty term that enforces spatial closeness between pixels in a variable manner. Furthermore, to further improve boundary preservation while maintaining efficiency, an additional penalty term that penalizes gradient differences can be incorporated into the ROFTV model, as large gradient differences are indicative of boundary crossings between two classes or regions.

Based on the aforementioned motivations, in the proposed ETVOS approach, we extend upon the existing ROFTV model with two additional total variation penalty weight terms: 1) a penalty weight term that enforces spatial closeness and 2) a penalty weight term that penalizes gradient differences. These additional penalty weight terms are incorporated to better reflect the task of SAR sea-ice image segmentation, where we wish to preserve the boundaries between different sea-ice types under the presence of high speckle noise. The first additional total variation penalty weight term introduced into the extended model is the spatial difference term denoted by $\omega_d(i,j)$ which enforces spatial closeness since spatially distant pixels are less likely to belong to the same sea-ice region. Note that the spatial difference term is modeled with Gaussian functions based on the numerous experimental tests and can be further expressed as

$$\omega_d(i,j) = e^{-\frac{1}{2}\left(\frac{\|i-j\|^2}{\sigma_d^2}\right)}. \tag{3}$$

The term $\omega_d(i,j)$ penalizes the spatial distance between pixels so that homogeneity of surrounding pixels is enforced. The term σ_d is the standard deviation for pixel difference, and as its value gets larger, the stronger spatial closeness is enforced.

The second additional penalty weight term introduced into the extended model is the gradient difference weight term denoted by $\omega_k(i,j)$, which enforces low gradient differences since pixels with large gradient differences are less likely to belong to the same region. Similar to the spatial difference penalty weight term, the gradient difference between pixels can be modeled and further articulated as

$$\omega_k(i,j) = e^{-\frac{1}{2}\left(\frac{\|k(i)-k(j)\|^2}{\sigma_k^2}\right)} \tag{4}$$

where $k(i)$ and $k(j)$ are the gradients at two interacting pixels i and j, respectively. The term σ_k denotes the standard deviation of the gradient difference between pixels. Similar to the mechanism built for computing an intensity difference, the gradient difference is enforced between pixels since large gradient differences will have a smaller likelihood of belonging to the same class.

Therefore, with these additional weighting penalties, the final discrete formulation of the SAR image segmentation problem based on the proposed extended ROFTV model can be written as

$$\hat{u} = \arg\min_{u} \left[\alpha \sum_i |\log f(i) - \log u(i)|^2 + \beta \sum_i \sum_j \omega_d(i,j)\omega_k(i,j)\,|u(i) - u(j)| \right]. \tag{5}$$

As can be seen in (5), the spatial and gradient penalty weight terms $\omega_d(i,j)$ and $\omega_k(i,j)$, respectively, have been incorporated to the extended ROFTV model to better estimate the piecewise constant where classes can be easily separable. To solve this problem in an efficient manner, an iterative weighted optimization strategy known as the diagonal normalized steepest descent (DNSD) algorithm is employed to approximate u. Details regarding the implementation of the DNSD algorithm used in the proposed method can be found in [26] and [27].

Theoretically, running the optimization detailed in (5) to convergence would provide us with the piecewise constant state that represents the segmented image u. However, from a practical perspective, running this strategy to convergence to achieve steady state can be computationally expensive. However, throughout the course of numerous tests, it has been found that even running a limited number of iterations can provide good approximations of the piecewise constant state. Fig. 2(a) and (b) shows the products of the first phase of the proposed ETVOS method utilizing all three penalty terms as noted earlier and the standard ROFTV model, respectively, for the scene shown in Fig. 1(a). The statistical distribution of Fig. 2(a) drawn from the proposed method clearly demonstrates that the rough approximation of the piecewise constant state has a multimodal shape, indicating that the inherent image noise and other artifacts have been significantly eliminated. On the other hand, the statistical distribution of Fig. 2(b) obtained from using the standard ROFTV method shows an improved but still largely unimodal shape indicating that there is considerable less statistical discrimination between the different classes. These results indicate that the inclusion of the additional penalty terms helps provide better class discrimination when handling SAR imagery. Such a comparison shows that the proposed ETVOS provides better statistical class delineation than the standard ROFTV by taking two additional total variation constraints made specifically for addressing the SAR image segmentation problem.

Since the approximation of the piecewise constant state has a multimodal shape as shown in Fig. 2(a), a faster alternative global classification strategy can now be employed on the results from Phase I to determine the final segmented results. Motivated by this observation, the proposed method utilizes a finite mixture model classification strategy in the second phase to determine the final segmented results based on the results from Phase I.

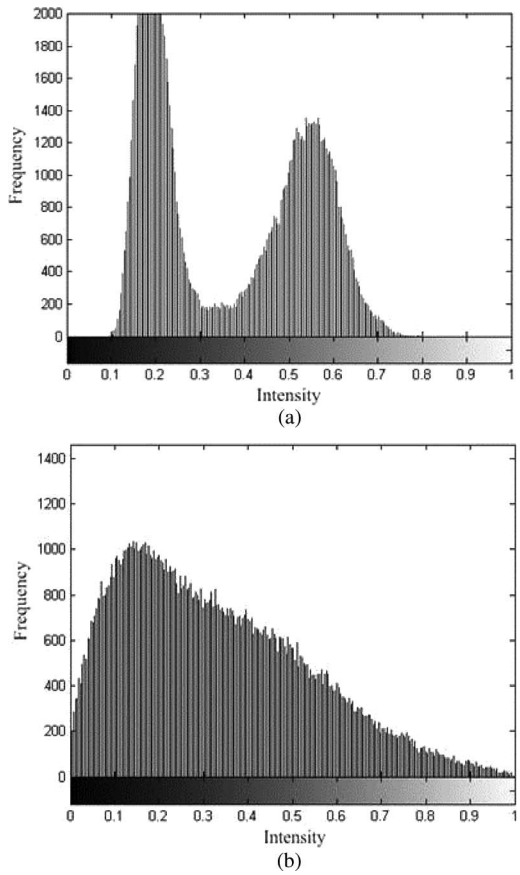

Fig. 2. Histograms generated from the application of the first phase using (a) the proposed ETVOS method and (b) the standard ROFTV method for the scene shown in Fig. 1(a).

B. Phase II—Finite Mixture Model Classification

In Phase II, a GMM is employed to find how many different classes there are and their associated parameters in the approximation of the piecewise constant $\hat{u}$. Let n be the number of components within the mixture model.

Furthermore, let l be a class label, where $l \in 1, \ldots, n$, and Θ be the set of parameters to be estimated for the mixture model

$$\Theta = \{\mu_1, \ldots, \mu_n, \sigma_1, \ldots, \sigma_n, P(u=1), \ldots, P(u=n)\} \quad (6)$$

where μ, σ, and $P(u)$ denote the mean at the center of each Gaussian distributed parabola, standard deviation, and prior probability of an observed subclass component within the mixture model, respectively. The goal is to precisely model the underlying distribution. With such a model, the probability of observing $\hat{u}$ can be expressed by

$$P(\hat{\mu}|\Theta) = \sum_{j}^{n} p(\hat{u}, l=i|\Theta). \quad (7)$$

To estimate Θ, expectation maximization (EM) [28] is performed as follows:

$$\Theta_{t+1} = \arg\max_{\Theta} \sum_{j=1}^{m} \sum_{i=1}^{n} (l_j = i|\hat{u}_j, \Theta_t) \ln p(l_j = i, \hat{u}j|\Theta) \quad (8)$$

where

$$p(l_j = i|\hat{u}_j, \Theta_t) = \frac{p(\hat{u}_j|l_j = I, \Theta_t)P(l_j = i|\Theta_t)}{\sum_{v=1}^{n} p(\hat{u}_j|l_j = v, \Theta_t)P(l_j = v|\Theta_t)} \quad (9)$$

is the probability of the label for pixel j having a class label index i, given the piecewise constant state u and set of parameters Θ, t denotes the iteration, v indicates a dummy variable, and m and n represent the number of pixels in the image and the number of components within the mixture model, respectively.

Finally, once unknown parameters are determined using EM, the maximum likelihood (ML) estimate of the final class l (target area or nontarget area) at pixel $\underline{x}$ can be obtained by calculating the following:

$$\hat{l}(\underline{x}) = \arg\max_{l} p\left(\hat{u}(\underline{x})|l\right). \quad (10)$$

III. Experimental Results

A RADARSAT-2 image covering a sea area nearby the Province of Newfoundland, Canada, was used in this study, as seen in Fig. 3(a), since it contained various sea-ice types that have been verified by trained sea-ice analysts at CIS. The image was acquired in the HH polarization mode using ScanSAR Wide beam with the full incidence angle range of 20° to 49° at 22:29:36 on March 16, 2009, and its spatial resolution had been degraded to 100 m for the enhancement of sea ice, which is ideal for sea-ice detection. Due to a large size of the original image (4239 by 4221 pixels), a smaller subset of this image was used to enable a relatively shorter processing time. To have a better understanding of the data set, each distinct region has been labeled as land, ocean, and sea ice as shown in Fig. 3(a).

To validate the proposed algorithm in detecting various sea-ice types in a more convincing fashion, the analytical data that confirms sea-ice types was necessary. The CIS website has an archive in which daily regional ice charts are available as shown in Fig. 3(b). The regional ice chart provides the series of egg codes in a simple oval form, which details the sea-ice concentrations, stages of development, and form of the ice for each segment of sea-ice-covered regions [29]. By carefully analyzing the egg codes for each segment of the study area, it was found that there were mainly two different types of sea ice presented: 1) "Egg-Code 4" representing gray ice with a thickness of 10–15 cm and 2) "Egg-Code 1" representing medium first-year ice with a thickness of 70–120 cm. However, the egg code does not give more detailed local-scale information such as where exactly the gray ice and the first-year medium ice are located within each segment. Thus, different sea-ice types present in the data set in a smaller scale (within each segment) were analyzed from the theoretical aspect as an alternative approach along with the information obtained from investigating the regional ice chart confirming that there are two different sea-ice types on the area of interest.

SAR backscatter in sea-ice imagery depends on the surface roughness and the dielectric constant of sea ice or open seawater [12]. The dielectric constant of sea ice decreases as the

(a)

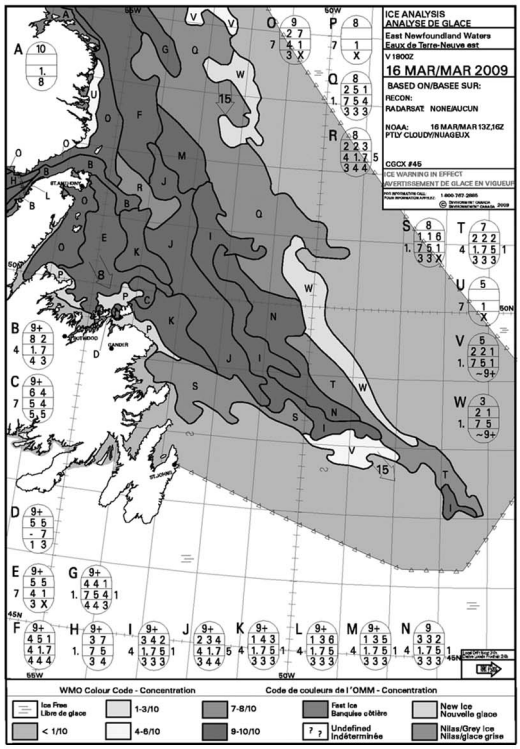

(b)

Fig. 3. (a) RADARSAT-2 sea-ice image. (b) Daily regional ice-chart covering study area.

degree of salinity decreases. If there is a lower dielectric constant, then the amount of backscattering is high. This implies that the thicker sea ice will tend to be brighter in color because its salinity is near zero. On the other hand, new or fresh sea ice tends to be darker in the image since it has a higher dielectric constant; as a result, the amount of backscattering is low. Knowing how various sea-ice types appear in the SAR imagery and with additional knowledge obtained from investigating the egg codes, the number of different sea-ice types can be carefully determined. Fig. 4 shows a subset taken from a concentrated sea-ice region.

As shown in Fig. 4, three main classes can be extracted from the subset of the image: The circles indicate the relatively thicker ice, possibly being medium first-year ice with a thickness of 70–120 cm (observed higher backscatter return); the triangles indicate the fresh/thin ice, possibly being gray ice with a thickness of 10–15 cm (observed lower backscatter return); and the rectangles identify the seawater (observed very low or no backscatter return). It is important to emphasize that three distinctive classes have been categorized by means of visual inspection with the aid of prior knowledge including varying surface feature characteristics to SAR signals and analysis of egg codes as discussed previously to help make the right decision. However, the authors want to point out that such analysis can be slightly different from reality. For example, the regions in rectangles could possibly be covered with very thin ice that appears to be equally dark as the seawater. In order to determine whether the detected feature is purely seawater or a very thin ice-covered region, sample intensity values of the seawater were collected from the other part of the same image and compared with the intensity values extracted from the regions in rectangles, where their intensity values were found to be similar; hence, it was concluded that the detected feature was seawater. Unless there are additional data revealing what regions were actually present at the time of the image acquisition, analysis has to be done using both the underlying signal difference characteristics of various sea-ice types and seawater and prior knowledge from examining the ice chart containing egg codes. To support this method, even trained sea-ice experts at CIS rely on visual inspection and backscattered values as was done in this paper. Thus, making reliable assumptions based on visual inspection and other conceptual-based knowledge is regarded as very important in sea-ice analysis.

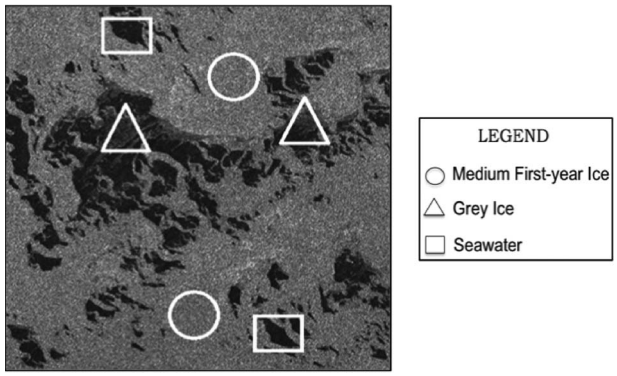

Fig. 4. Subset taken from the sea-ice region.

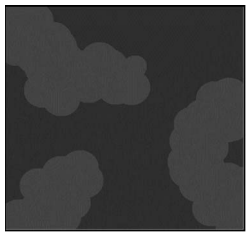

Fig. 5. Synthetic sea-ice image.

A. Experiment I—Using Synthetic Data Under Noise

In this paper, the performance of ETVOS under various noise levels was investigated using synthetic data. A synthetic

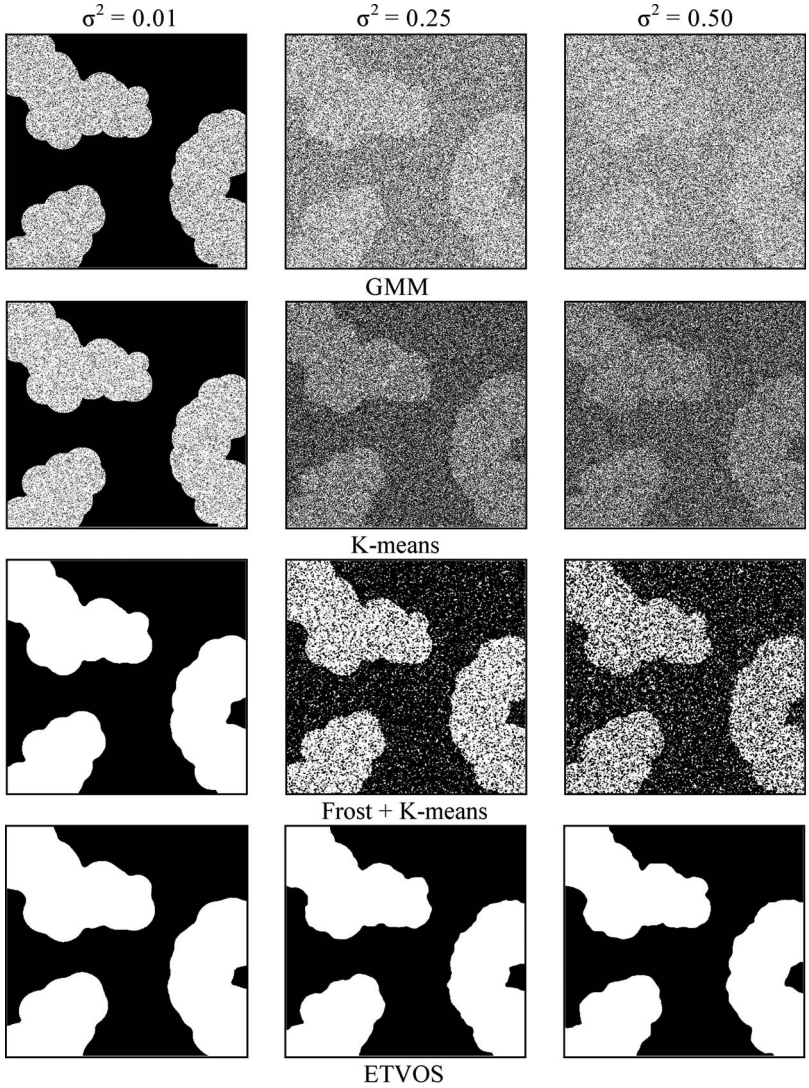

Fig. 6. Segmentation results on a synthetic image at different speckle noise levels using four methods.

sea-ice image was created for this experiment, consisting of two different gray levels representing seawater and sea ice, as shown in Fig. 5.

To validate the effectiveness and the robustness of the proposed algorithm under noise, multiplicative speckle noise at 11 different noise levels has been applied, ranging between $\sigma^2 = 0.01$ and $\sigma^2 = 0.50$ (increase at an increment of 0.05). The methods used to compare with the proposed ETVOS include the widely used global segmentation methods that are based on the K-means clustering [10] and GMM [13]. In addition to these two methods, we also applied one additional segmentation scheme. According to [30], the segmentation performance can be improved significantly when applying a speckle filter such as Lee [14], Kuan [15], and Frost [16] followed by K-means clustering. These speckle filters have been well recognized for their effectiveness and robustness; as a result, they are currently available in almost all remote sensing software packages. As such, the Frost filter was utilized to first eliminate speckle noise, and then, K-means clustering was used to segment each class in SAR sea-ice imagery.

Fig. 6 shows the comparisons of segmentation results using three methods including K-means, GMM, and Frost $+$ K-means with the proposed ETVOS method and shows how each method performs under different speckle noise levels. The test images carried artificial speckles with variances of 0.01, 0.25, and 0.50 at low, mid, and high noise levels, respectively.

As shown in Fig. 6, the proposed ETVOS method outperforms the rest of the three other methods. As the severity of speckle noise embedded in the synthetic image increases, it is well observed that the rest of the methods fail to segment two distinct classes. Also, note that GMM and K-means segmentation methods fail to an extreme extent. This is mainly due to their segmentation schemes that only take a global tonal characteristic into account making them very weak in removing speckle noises. On the other hand, the segmentation results derived from our proposed method well differentiates two classes. Such strong results are obtained due to the three penalty terms that were incorporated into the extended ROFTV model, with the spatial difference penalty term helping to deal with speckle noise, while the intensity and gradient difference penalty terms

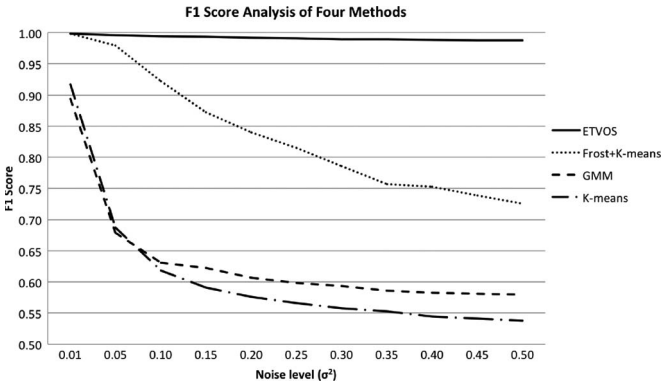

Fig. 7. F1 score for comparison of four methods at varying noise levels.

help to well preserve boundaries. Hence, the segmentation results using a synthetic test image under different noise levels help to illustrate the effectiveness and the robustness of the proposed ETVOS method.

To see these results shown in Fig. 6 in a quantitative fashion, we have performed the F1 score test, which is widely used to validate the accuracy of test data. It also provides a good measure of how each test method performs under different environments (in our case, different test methods and noise levels). The general formula for F1 score derived based on van Rijsbergen's effectiveness measure [31] can be expressed by

$$F_1 = \frac{2TP}{2TP + FN + FP} \tag{11}$$

where TP, FP, and FN denote true positive, false positive, and false negative, respectively. By implementing F1 score test, we can observe how accurately the segmentation results are matched with the ground truth image (the original synthetic image) whose F1 score value varies between zero being absolutely no match and one being a perfect match.

Fig. 7 summarizes the F1 scores of four different methods at varying speckle noise levels.

It can be observed that the F1 score analysis illustrates the improved segmentation accuracy of the ETVOS method in a quantitative fashion over the other tested segmentation methods. Notice that F1 score of the proposed ETVOS method shows the relatively consistent pattern as shown in flat line whereas F1 score derived from other methods decreases as the amount of embedded noise σ^2 increases. This drop is particularly noticeable for K-means and GMM, as both experienced a dramatic fall between the σ^2 values of 0.01 and 0.05. The Frost $+$ K-means segmentation method shows a relatively better performance than those two without having F1 values to drop quickly. However, its relatively better segmentation performance gets poorer as the noise level increases. Through the quantitative validation with respect to its original synthetic image, the proposed ETVOS approach has been demonstrated to provide strong segmentation accuracy under high speckle noise.

B. Experiment II—Using Real SAR Sea-Ice Imagery

In this section, experimental results of the proposed ETVOS method, along with three other methods (GMM, K-means, and Frost $+$ K-means) on real SAR sea-ice imagery, are presented along with discussions stating which methods produce more promising result. Testing of the proposed method and other methods listed were performed on four test subsets of RADARSAT-2 sea-ice imagery, which are shown in Fig. 8. The size and the number of classes that were seen from the four test subsets are described in Table I. It is important to note that the number of classes has been determined strictly by visual inspection with underlying knowledge of sea-ice characteristics and egg-code analysis as described earlier.

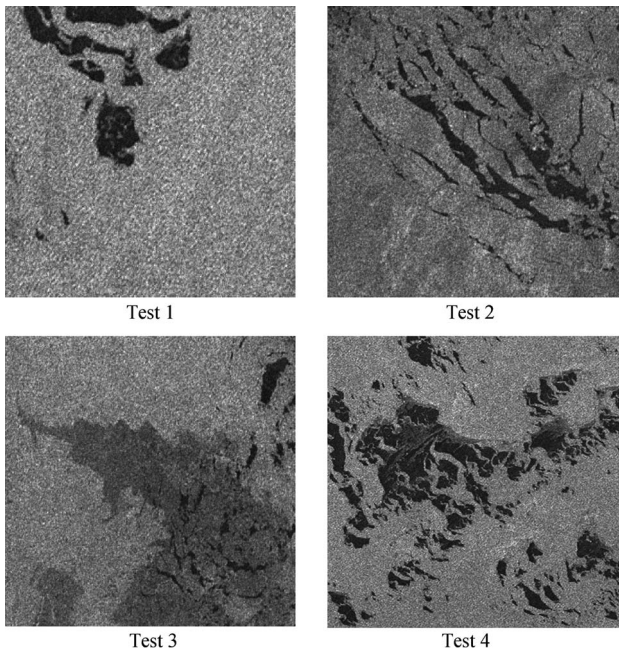

Fig. 8. Subsets of real RADARSAT-2 SAR sea-ice imagery used for testing.

TABLE I
SUMMARY OF TESTED IMAGES

	Size of image (pixels)	Observed number of classes
Test 1	277 x 259	2 (medium first-year sea-ice & seawater)
Test 2	349 x 340	2 (medium first-year sea-ice & seawater)
Test 3	384 x 348	3 (grey sea-ice, medium first-year sea-ice & seawater)
Test 4	505 x 525	3 (grey sea-ice, medium first-year sea-ice & seawater)

Fig. 9 shows the segmentation results of the proposed ETVOS method and three aforementioned segmentation methods using four test images. The overall segmentation results produced by GMM clustering, K-means, and Frost $+$ K-means show that, while the boundaries of sea-ice areas and seawater are visible, they appear very noisy. The general impression of the results obtained by K-means and GMM clustering approaches is particularly noisy, and such a poor performance is due to the fact that they are global segmentation methods, which only consider global tonal characteristics making them very sensitive to speckle noise while ignoring local spatial relationships. On the other hand, the segmentation results produced by the proposed ETVOS method well preserved the boundaries of seawater and sea ice in all tests. The segmentation results that are derived from the combination of the well-known Frost denoising filter with K-means have

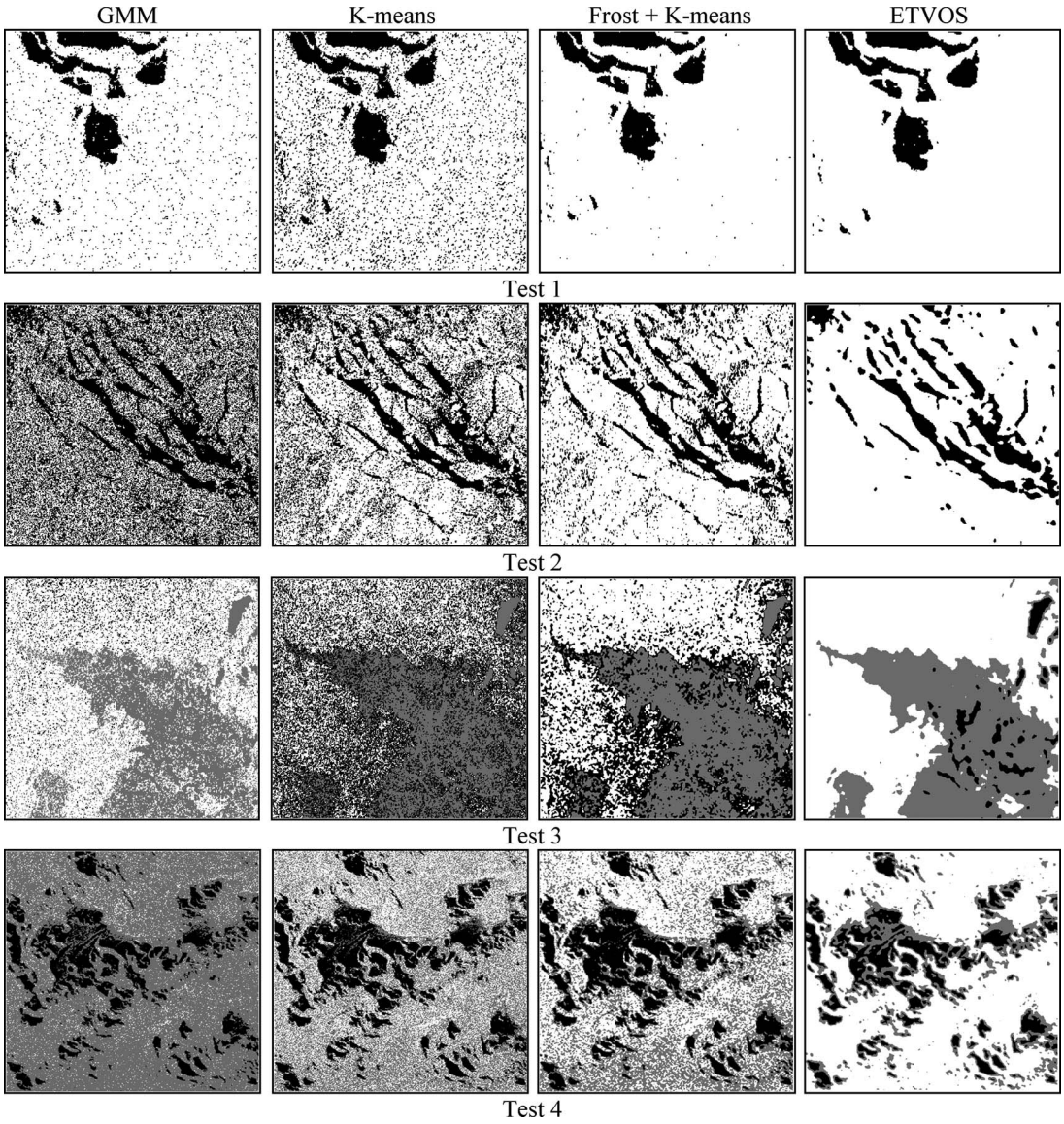

Fig. 9. Segmentation results on four test sets of real SAR sea-ice imagery using the tested methods.

proved their effectiveness by Marques *et al.* who showed that it could bring a noticeable improvement when compared to using K-means by itself. This is true to some extent when analyzing Tests 1 and 2 when the Frost filter was somewhat sufficient to suppress the underlying noise distribution, although the final segmentation results still contain an ample amount of random noise. On the other hand, the ETVOS evidently segmented two regions containing medium first-year sea ice and seawater as demonstrated in the results of Tests 1 and 2. For Tests 3 and 4, the three other test methods performed poorly when three different classes were present. Since the intensity variation of pixels between gray sea ice and medium first-year sea ice is low, all other segmentation methods except for the proposed ETVOS failed to define each different class in an accurate manner; rather, they often confused medium first-year sea ice with gray sea ice as illustrated by many wrongly classified pixels. Furthermore, results drawn from three other methods for Test 3 show that gray sea ice and seawater are completely mixed as one homogeneous region. This occurs mainly due to the inadequate ability of defining the intensity/gradient differences within two regions failing to pick out two analogous intensity values. Moreover, a supposedly homogeneous region containing, for instance, first-year sea ice in all four test images, has been misclassified mostly as seawater due to the insufficient capability of defining the spatial closeness to enforce the homogeneity within the region. This is mainly due to the absence of spatial difference penalty term. Conversely, the proposed ETVOS equipped with three penalty constraints was able to amply reduce the overall noise level and satisfactorily segment regions in a desired manner.

The proposed ETVOS method well supports its possibility to be applied for operational use, as the processing time was short, approximately 8, 12, 16, and 31 s for test subsets 1, 2, 3, and 4, respectively. The computer used for the testing is equipped with Intel dual-core CPUs at 2.4 GHz and 3 GB of RAM. Therefore, it was shown that the proposed ETVOS approach produces superior results compared to other methods.

IV. Conclusion

This paper has introduced a novel SAR sea-ice image segmentation algorithm called ETVOS. This approach first uses an extended total variation optimization phase to construct the piecewise constant state via three total variation constraints. After the classes in the piecewise constant state has become clearly separable, an EM approach is then utilized to learn a GMM. Finally, an ML classification is performed to assign each pixel into a final class. Based on our experimental results, the proposed method produces a very satisfactory result when compared to other well-established methods. Although a longer processing time is required when incorporating the texture information of sea ice to the proposed ETVOS method, it can be beneficial in helping to better analyze images with multiple sea-ice types. Thus, the study of efficient implementation algorithm combining texture characteristics with the proposed method is highly recommended for future work.

Acknowledgment

The authors would like to thank the Canadian Ice Service for providing RADARSAT-2 images for evaluation. They would also like to thank anonymous reviewers for their helpful suggestions in making this paper a better presentation.

References

[1] J. A. Nystuen and F. W. Garcia, Jr., "Sea ice classification using SAR backscatter statistics," *IEEE Trans. Geosci. Remote Sens.*, vol. 30, no. 3, pp. 502–509, May 1992.

[2] A. Carlstrom, "A microwave backscattering model for deformed first-year sea ice and comparisons with SAR data," *IEEE Trans. Geosci. Remote Sens.*, vol. 35, no. 2, pp. 378–391, Mar. 1997.

[3] W. Dierking and T. Busche, "Sea ice monitoring by L-band SAR: An assessment based on literature and comparisons of JERS-1 and ERS-1 imagery," *IEEE Trans. Geosci. Remote Sens.*, vol. 44, no. 4, pp. 957–970, Apr. 2006.

[4] W. Dierking and J. Dall, "Sea-ice deformation state from synthetic aperture radar imagery—Part I: Comparison of C- and L-band and different polarization," *IEEE Trans. Geosci. Remote Sens.*, vol. 45, no. 11, pp. 3610–3622, Nov. 2007.

[5] W. Dierking and J. Dall, "Sea ice deformation state from synthetic aperture radar imagery—Part II: Effects of spatial resolution and noise level," *IEEE Trans. Geosci. Remote Sens.*, vol. 46, no. 8, pp. 2197–2207, Aug. 2008.

[6] W. Dierking, "Mapping of different sea ice regimes using images from sentinel-1 and ALOS synthetic aperture radar," *IEEE Trans. Geosci. Remote Sens.*, vol. 48, no. 3, pp. 1045–1058, Mar. 2010.

[7] N. Otsu, "A threshold selection method from grey-level histogram," *IEEE Trans. Syst. Sci. Cybern.*, vol. SMC-9, no. 1, pp. 62–66, Jan. 1979.

[8] D. Havercamp, L. Soh, and C. Tsatsoulis, "A dynamic local thresholding technique for sea ice classification," in *Proc. IGARSS*, Aug. 1993, vol. 2, pp. 638–640.

[9] R. Samadani, "A finite mixture algorithm for finding proportions in SAR images," *IEEE Trans. Image Process.*, vol. 4, no. 8, pp. 1182–1186, Aug. 1995.

[10] Q. Redmund, D. Long, and M. Drinkwater, "Polar sea-ice classification using enhanced resolution NSCAT data," in *Proc. IGARSS*, Jul. 1998, vol. 4, pp. 1976–1978.

[11] J. Karvonen, "Baltic sea ice SAR segmentation and classification using modified pulse-coupled neural networks," *IEEE Trans. Geosci. Remote Sens.*, vol. 42, no. 7, pp. 1566–1574, Jul. 2004.

[12] D. Deng and D. A. Clausi, "Unsupervised segmentation of SAR sea ice imagery using a novel Markov random field model," *IEEE Trans. Geosci. Remote Sens.*, vol. 43, no. 3, pp. 528–538, Mar. 2005.

[13] M. Alf, L. Nieddu, and D. Vicari, "A finite mixture model for image segmentation," *Stat. Comput.*, vol. 18, no. 2, pp. 137–150, Jun. 2008.

[14] J. S. Lee, "Digital image enhancement and noise filtering by use of local statistics," *IEEE Trans. Pattern Anal. Mach. Intell.*, vol. PAMI-2, no. 2, pp. 165–168, Mar. 1980.

[15] D. Kuan, A. Sawchuk, T. Strand, and P. Chavel, "Adaptive restoration of images with speckle," *IEEE Trans. Acoust., Speech, Signal Process.*, vol. ASSP-35, no. 3, pp. 373–383, Mar. 1987.

[16] V. Frost, J. Stiles, K. Shanmugan, and J. Holtzman, "A model for radar images and its application to adaptive digital filtering of multiplicative noise," *IEEE Trans. Pattern Anal. Mach. Intell.*, vol. PAMI-4, no. 2, pp. 157–166, Mar. 1982.

[17] Y. Yu and S. Acton, "Speckle reducing anisotropic diffusion," *IEEE Trans. Image Process.*, vol. 11, no. 11, pp. 1260–1270, Nov. 2002.

[18] D. A. Clausi, "An analysis of co-occurrence texture statistics as a function of grey level quantization," *Can. J. Remote Sens.*, vol. 28, no. 1, pp. 45–62, Feb. 2002.

[19] D. G. Barber and E. F. LeDrew, "SAR sea ice discrimination using texture statistics: A multivariate approach," *Photogramm. Eng. Remote Sens.*, vol. 57, no. 4, pp. 385–395, 1991.

[20] L.-K. Soh and C. Tsatsoulis, "Texture analysis of SAR sea ice imagery using gray level co-occurrence matrices," *IEEE Trans. Geosci. Remote Sens.*, vol. 37, no. 2, pp. 780–795, Mar. 1999.

[21] D. A. Clausi and B. Yue, "Comparing co-occurrence probabilities and Markov random fields for texture analysis of SAR sea ice imagery," *IEEE Trans. Geosci. Remote Sens.*, vol. 42, no. 1, pp. 215–228, Jan. 2004.

[22] R. Chellappa and S. Chatterjee, "Classification of texture using Gaussian Markov random fields," *IEEE Trans. Acoust., Speech, Signal Process.*, vol. ASSP-33, no. 4, pp. 959–963, Aug. 1985.

[23] Q. Yu and D. A. Clausi, "SAR sea-ice image analysis based on iterative region growing using semantics," *IEEE Trans. Geosci. Remote Sens.*, vol. 45, no. 12, pp. 3919–3931, Dec. 2007.

[24] L. Evans and R. Gariepy, *Measure Theory and Fine Properties of Functions*. Boca Raton, FL: CRC Press, 1992.

[25] L. I. Rudin, S. Ohser, and E. Fatemi, "Nonlinear total variation based noise removal algorithms," *Phys. D*, vol. 60, no. 1–4, pp. 259–268, Nov. 1992.

[26] D. Bertsekas, *Nonlinear Programming*. Belmont, MA: Athena Scientific, 1995.

[27] D. Luenberger, *Linear and Non-Linear Programming,* 2nd ed. Reading, MA: Addison-Wesley, 1987.

[28] A. Dempster, N. Laird, and D. Rubin, "Likelihood from incomplete data via the EM algorithm," *J. R. Stat. Soc., Ser. B*, vol. 39, no. 1, pp. 1–38, 1977.

[29] Environment Canada, The Egg Code, accessed on 18 August 2011. [Online]. Available: http://www.ec.gc.ca/glaces-ice/default.asp?lang=En&n=84F6AA59-1&wsdoc=FE5C2688-21A8-4165-8FFB-5D28B2A1D943

[30] R. C. P. Marques, E. A. Carvalho, R. C. S. Costa, and F. N. S. Medeiros, "Filtering effects on SAR images segmentation," *Lecture Notes in Computer Science*, vol. 3124, pp. 1041–1046, 2004.

[31] C. J. van Rijsbergen, *Information Retrieval,* 2nd ed. Woburn, MA: Butterworth-Heinemann, 1979.

Tae-Jung Kwon received the B.Eng. degree in civil engineering with geomatics engineering option from Ryerson University, Toronto, ON, Canada, in 2009 and the M.Sc. degree in geomatics from the University of Waterloo, Waterloo, ON, in 2011, where he is currently working toward the Ph.D. degree in the Department of Civil and Environmental Engineering with specialization of transportation engineering.

His current research interests are in the areas of winter road maintenance, more specifically in weather and surface sensor evaluation, road surface condition estimation and forecasting, and optimization of road weather information systems density and location through integration of digitally processed satellite images.

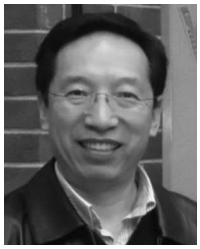

Jonathan Li (M'00–SM'11) received the Ph.D. degree in geomatics engineering from the University of Cape Town, Cape Town, South Africa, in 2000.

He has been with the Key Laboratory of Underwater Acoustic Communication and Marine Information Technology of the Ministry of Education, Xiamen University, Xiamen, China, since 2011 and has been a Professor with the Department of Geography and Environmental Management, University of Waterloo, Waterloo, ON, Canada. He has published more than 180 papers in refereed journals, books, and proceedings and coedited six books and six theme issues. His current research interests are in the areas of remote sensing of inland and coastal waters, renewable energy potential, and critical infrastructure.

Dr. Li was the recipient of the 2011 Talbert Abrams Award for Best Paper in Photogrammetry and Remote Sensing, the 2008 Environmental Systems Research Institute Award for Best Paper in Geographic Information Science, and the 2006 MacDonald, Dettwiler and Associates Ltd. Award for Best Paper in Photogrammetry and Hydrography. He is the Chair of the International Society for Photogrammetry and Remote Sensing Intercommission Working Group on Land-Based Mobile Mapping Systems (2008–2012), the Vice Chair of the International Cartographic Association Committee on Mapping from Remote Sensor Imagery (2011–2015), and the Vice Chair of the International Federation of Surveyors Commission on Hydrography (2011–2014).

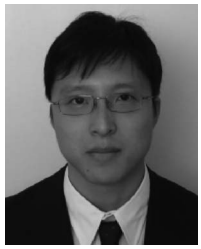

Alexander Wong (M'05) received the B.Sc. degree in computer engineering, the M.Sc. degree in electrical and computer engineering, and the Ph.D. degree in systems design engineering from the University of Waterloo, Waterloo, ON, Canada, in 2005, 2007, and 2010, respectively.

Since 2011, he has been an Assistant Professor with the Department of Systems Design Engineering, University of Waterloo, where he is also a Codirector of the Vision and Image Processing Research Group. He is involved in various projects on image registration, image denoising, image superresolution, image segmentation, biomedical tracking, biomedical image analysis, and image and video coding. He has authored over 130 refereed papers, books, and patents in these areas. His current research interests include biomedical image processing and analysis, computer vision, and pattern recognition.

Dr. Wong is the recipient of the Best Paper Award by the Canadian Image Processing and Pattern Recognition Society, an Early Researcher Award from the Ministry of Economic Development and Innovation, an Outstanding Performance Award, and an Alumni Gold Medal.